Linear analysis of engine core noise using a hybrid modeling approach

By J. Kim, J. O'Brien AND M. Ihme

1. Motivation and objectives

Reducing noise generated by gas-turbine engines has been one of the major practical interests of engine manufacturers and the aviation industry. Radiated sound from gas-turbine engines (such as modern turbofan engines) is often broken into several components for analysis – fan noise, compressor noise, combustor noise, and jet noise – with jet noise dominating the others at high-speed operating conditions. Core noise is defined as any excess noise generated within the engine core. Its generation is often associated with the combustion process and the convection of high-temperature gas (Strahle 1978; Hubbard 1991; Motheau *et al.* 2014). Core noise is attributed to an important noise source at low frequencies of $O(10^2)$ Hz. Over the past several decades, significant progress has been made in reducing jet noise and fan noise, both of which have increased the relative importance of core noise. Also, at low-speed operating conditions where jet noise is less prominent (for example, aircraft during taxi and approach, industrial gas turbine, and auxiliary power unit), core noise can be significant.

Noise generated within the combustor, or direct core noise, is often reflected and scattered through the turbine stages, where it can propagate back into the combustion chamber. This can potentially trigger acoustic resonances which may lead to thermo-acoustic instabilities. In addition to direct core noise, high-temperature combustion products undergo significant acceleration while propagating through the turbine stages and exhaust nozzle, a process which can convert some of the entropy and vorticity fluctuations into noise. This process, often termed indirect noise (Strahle 1978), can significantly impact the sound radiation of gas-turbine engines at high-speed conditions (Muthukrishnan *et al.* 1978; Leyko *et al.* 2009). Since aircraft engines typically operate in this regime (due to the substantial acceleration in the turbine stages and exhaust nozzle), the indirect mechanism is likely to dominate core noise in aviation gas turbines (Strahle 1978).

Understanding the fundamental mechanisms of core-noise generation and propagation is an essential step toward further reducing the overall noise from gas-turbine engines. It is also important to understand how core noise interacts with the engine components, since its generation and propagation can be closely linked with thermo-acoustic instabilities in the combustor.

While high-fidelity simulation based upon large-eddy simulation (LES) has proven useful in modeling high-speed, high-temperature turbulent flows, it is still expensive to directly apply this technique throughout the entire flow-path of gas-turbine engines. In portions of the flow-path, there is still a need to use simpler models that offer sufficiently accurate predictions at reduced computational costs, while high-fidelity simulation can be used as required where flow complexities are significant. The appropriate balance of these hybrid techniques can provide insight into the underlying mechanisms of core-noise generation and propagation at sustainable computational costs.

In this study, we investigate fundamental core-noise mechanisms in a modeled gas-

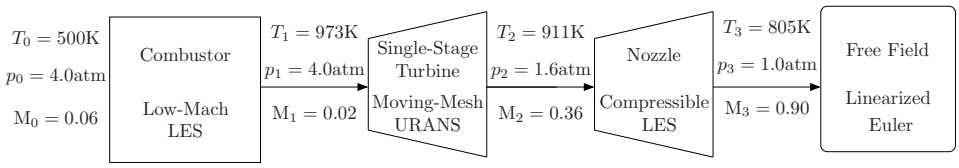

FIGURE 1. Summary of the prediction models and thermodynamic states for the flow-path of the representative gas-turbine engine.

turbine flow-path that contains essential components of a commercial jet engine at a cruise condition. To this end, a hybrid modeling approach is used, which combines high-fidelity simulation and lower-order prediction tools. A canonical engine core is designed, consisting of a combustor, a single-stage turbine, and a converging nozzle. See *et al.* (2012) studied a similar configuration without a turbine stage. The reactive flow within the combustor is modeled using LES based upon a low-Mach-number formulation of the full Navier–Stokes equations. The downstream characteristics from the combustor are then fed into the turbine-stage simulation (a one-way, downstream-only coupling). The turbine stage is predicted using a fully compressible Unsteady Reynolds-Averaged Navier–Stokes (URANS) code with moving-mesh capabilities to account for the relative motion of the rotor and stator. The turbine-stage simulation predicts the evolution of the disturbances originating from the combustor, which are then used to perturb the base state of the downstream nozzle flow. A linear model is adopted to investigate the development of the upstream disturbances and their acoustic signature at the far field. The hybrid model as well as the thermodynamic states of the engine flow-path are illustrated in Figure 1.

2. Physical and numerical models

2.1. *Combustor simulation*

The combustor stage is modeled using the code Vida†, an LES solver that has previously been validated in similar applications (See & Ihme 2014). VIDA is a tool that solves the low-Mach-number formulation of the reacting Navier–Stokes equations on unstructured grids. The code is fully implicit and second-order accurate in time and space on arbitrary grids. The chemical source term is modeled by the flamelet progress variable approach using a three-dimensional chemistry table based on tabulated chemistry for methane–air diffusion flames. The filtered momentum equation is closed using the Vreman model, and the turbulent scalar fluxes are closed using a constant turbulent Schmidt number assumption. The resulting set of governing equations is

$$\frac{\partial \bar{\rho}}{\partial t} + \frac{\partial \bar{\rho}\widetilde{u}_j}{\partial x_j} = 0 \tag{2.1a}$$

$$\frac{\partial \bar{\rho}\widetilde{u}_i}{\partial t} + \frac{\partial \bar{\rho}\widetilde{u}_i\widetilde{u}_j}{\partial x_j} = -\frac{\partial \bar{p}}{\partial x_i} + \frac{\partial}{\partial x_j}\left[(\bar{\mu}+\mu_t)\left(\frac{\partial \widetilde{u}_i}{\partial x_j} + \frac{\partial \widetilde{u}_j}{\partial x_i} - \frac{2}{3}\delta_{ij}\frac{\partial \widetilde{u}_k}{\partial x_k}\right)\right] \tag{2.1b}$$

$$\frac{\partial \bar{\rho}\widetilde{Z}}{\partial t} + \frac{\partial \bar{\rho}\widetilde{u}_j\widetilde{Z}}{\partial x_j} = \frac{\partial}{\partial x_j}\left[\left(\bar{\rho}\widetilde{D} + \frac{\mu_t}{\mathrm{Sc}_t}\right)\frac{\partial \widetilde{Z}}{\partial x_j}\right] \tag{2.1c}$$

† http://www.cascadetechnologies.com/pdf/VIDA.pdf

$$\frac{\partial \bar{\rho}\widetilde{C}}{\partial t} + \frac{\partial \bar{\rho}\widetilde{u}_j\widetilde{C}}{\partial x_j} = \frac{\partial}{\partial x_j}\left[\left(\bar{\rho}\widetilde{D} + \frac{\mu_t}{\mathrm{Sc}_t}\right)\frac{\partial \widetilde{C}}{\partial x_j}\right] + \bar{\dot{\omega}}_c\left(\widetilde{Z}, \widetilde{C}\right) \tag{2.1d}$$

$$\frac{\partial \bar{\rho}\widetilde{Z''^2}}{\partial t} + \frac{\partial}{\partial x_j}\left(\bar{\rho}\widetilde{u}_j\widetilde{Z''^2}\right) = \frac{\partial}{\partial x_j}\left[\left(\bar{\rho}\widetilde{D} + \frac{\mu_t}{\mathrm{Sc}_t}\right)\frac{\partial \widetilde{Z''^2}}{\partial x_j}\right] - \left(2\bar{\rho}\widetilde{D}\frac{\partial \widetilde{Z}}{\partial x_j}\frac{\partial \widetilde{Z}}{\partial x_j} + \bar{\rho}C\widetilde{Z''^2}\frac{\mu_t}{\mathrm{Sc}_t\Delta^2}\right). \tag{2.1e}$$

2.2. *Turbine simulation*

The turbine stage is simulated using the in-house code SUMB, a fully compressible, unsteady RANS solver with moving-mesh capabilities. Structured, body-fitted grids are used to describe the geometry. The code is explicit and second-order accurate in time and space. SUMB has been validated in turbomachinery applications as part of the Center for Integrated Turbulence Simulations project (van der Weide *et al.* 2006). The inflow conditions are constructed by averaging the combustor simulation's outflow data to obtain the impinging characteristics, and the mean pressure is imposed from the interior of the turbine computational domain. The standard $k-\epsilon$ model is used for the turbulent closure. The treatment of the rotor–stator involves the construction of separate but adjacent meshes for each component, and the outflow of the upstream stage is mapped onto the inflow of the downstream stage to reflect the relative motion of the blades. Periodicity is employed to reduce computational costs; a small number of blades from each section (two from the stator and three from the rotor) are simulated with periodic boundary conditions representing the effects of the full cascade. Both the rotor and the stator are modeled as being infinitely long (zero radius of curvature), so the relative motion of the blades is linear translation.

2.3. *Nozzle-flow simulation*

The linearized Euler equations are used to predict the interaction of the upstream disturbances with the nozzle base flow and acoustic radiation to the far field. The compressible Euler equations for entropy, velocity, and pressure are non-dimensionalized using ambient quantities. The flow variables are decomposed into a time-stationary base state (denoted by an overbar) and fluctuations around the base state (denoted by a prime) as

$$q = \bar{q} + q'. \tag{2.2}$$

Substituting the decomposed variables and collecting the first-order terms of the fluctuating quantities, the linearized Euler equations are obtained as

$$\frac{\partial s'}{\partial t} + \bar{\boldsymbol{u}}\cdot\boldsymbol{\nabla}s' + \boldsymbol{u}'\cdot\boldsymbol{\nabla}\bar{s} = f_s \tag{2.3a}$$

$$\frac{\partial \boldsymbol{u'}}{\partial t} + \bar{\boldsymbol{u}}\cdot\boldsymbol{\nabla}\boldsymbol{u}' + \boldsymbol{u}'\cdot\boldsymbol{\nabla}\bar{\boldsymbol{u}} + \left(\frac{1}{\gamma}\frac{p'}{\bar{p}} - s'\right)\bar{\boldsymbol{u}}\cdot\boldsymbol{\nabla}\bar{\boldsymbol{u}} + \frac{1}{\bar{\rho}}\boldsymbol{\nabla}p' = f_{\boldsymbol{u}} \tag{2.3b}$$

$$\frac{\partial p'}{\partial t} + \bar{\boldsymbol{u}}\cdot\boldsymbol{\nabla}p' + \boldsymbol{u}'\cdot\boldsymbol{\nabla}\bar{p} + \gamma\left(\bar{p}\boldsymbol{\nabla}\cdot\boldsymbol{u}' + p'\boldsymbol{\nabla}\cdot\bar{\boldsymbol{u}}\right) = f_p, \tag{2.3c}$$

where s', $\boldsymbol{u}'$, and p' are entropy, velocity, and pressure fluctuations, respectively. The base state variables are prescribed and $\gamma = c_p/c_v = 1.4$ where c_p and c_v are the specific heats at constant pressure and volume, respectively. The right-hand side term $\boldsymbol{f} = (f_s, f_{\boldsymbol{u}}, f_p)^{\mathrm{T}}$

represents a general external forcing. The linearized equation of state is written as

$$\frac{T'}{\bar{T}} = \frac{p'}{\bar{p}} - \frac{\rho'}{\bar{\rho}}, \tag{2.4}$$

where the density fluctuation is computed by

$$\frac{\rho'}{\bar{\rho}} = \frac{1}{\gamma}\frac{p'}{\bar{p}} - s'. \tag{2.5}$$

The governing equations are directly solved for $\boldsymbol{q}' = \{s', \boldsymbol{u}', p'\}^{\mathrm{T}}$. The base state $\bar{\boldsymbol{q}}$ is obtained from a steady RANS simulation. The converged RANS solution is linearly interpolated to the grid for the linearized Euler simulation.

Spatial derivatives in the governing equations are transformed to curvilinear coordinates $\boldsymbol{\xi} = (\xi, \eta, \zeta)^{\mathrm{T}}$ using a non-singular mapping $\boldsymbol{x} = X(\boldsymbol{\xi}, \tau)$ with the inverse $\boldsymbol{\xi} = \Xi(\boldsymbol{x}, t)$. The transformation Jacobian, $J = \det(\partial\xi_i/\partial x_j)$, is positive definite. In this study, the mapping is time invariant and $\tau = t$.

The spatial discretization uses an eleven-point, explicit, wavenumber-optimized finite difference scheme (Bogey & Bailly 2004; Berland *et al.* 2007). The solution is time-advanced using the standard fourth-order Runge–Kutta method with a constant time-step size. For numerical stability, an eleven-point, explicit, optimized filter (Bogey & Bailly 2004) is applied at every time step in every direction. The filter strength is $\sigma_d = 0.2$. To minimize the impact of the filter, all filtered variables are averaged with the unfiltered variables as

$$q = \alpha q_{\mathrm{filtered}} + (1 - \alpha) q_{\mathrm{unfiltered}}, \tag{2.6}$$

where $0 \leq \alpha \leq 1$.

The computational domain for the linearized Euler simulations consists of multiple, overlapping blocks to represent mildly complex geometry such as a converging nozzle. In the present work, an overset-grid technique is applied to interpolate solution variables between two overlapping blocks. The fourth-order accurate interpolation stencils are generated at the pre-processing stage using Overture (Brown *et al.* 1999).

Boundaries which are not updated by the overset-grid interpolation are subject to physical boundary conditions. At the inflow, solution variables obtained from the upstream SUMB simulation are prescribed in space and in time. The characteristic, non-reflecting boundary conditions are applied at the outflow and at the far field (Poinsot & Lele 1992; Kim & Lee 2000). At solid walls, the no-penetration condition ($\boldsymbol{u} \cdot \hat{\boldsymbol{n}} = 0$) is applied, which is, in the inviscid limit, equivalent to the wall-normal pressure gradient being zero. To model the free-field radiation, an absorbing buffer zone is used (Freund 1997; Bodony 2006). The damping term has a quadratic distribution within the buffer zone with the damping constant of $\sigma = 0.5$.

3. Combustor and turbine simulation results

Preliminary results for the upstream combustor and turbine-stage simulations are shown, as simulations are still on-going. The combustor geometry considered is the dual-swirl gas-turbine combustor (Meier *et al.* 2007). Previous work has demonstrated the current code's capability to predict the turbulent reacting flow within the same combustor (See & Ihme 2014). To accommodate the full flow-path, the combustor simulation is run at a higher mass-flow rate and a fuel-leaner condition than has been studied experimentally. The mass-flow rate of air is 0.43 kg/s and the global equivalence ratio for

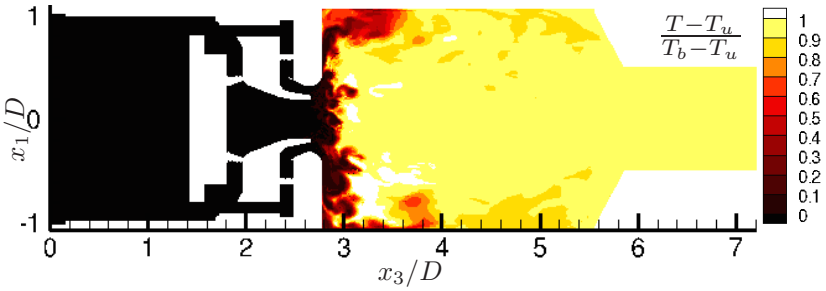

FIGURE 2. Instantaneous temperature in the gas-turbine combustor.

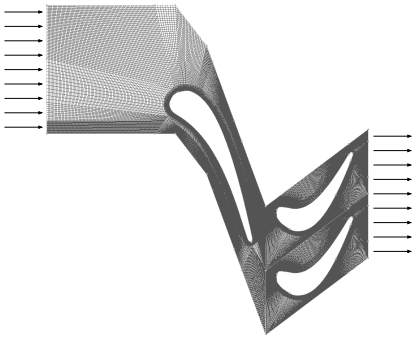

FIGURE 3. Computational domain and grid for the turbine-stage calculation.

methane combustion is 0.18. Air enters the combustor at 500 K and exits at 973 K. In the experimental work, the combustor has demonstrated two distinct behaviors: a flat-flame mode in which the flame remains attached to the wall and a V-flame where it is unattached. At this condition, the flat flame is observed, resulting in compact combustion and increased residence time for the burnt gases to mix before passing into the turbine. An instantaneous temperature field for the combustor simulation is illustrated in Figure 2, showing the presence of the flat-flame structure.

The turbine design considered in this study consists of a single rotor–stator pair taken from the NASA high-pressure turbine design (Stabe & Schwab 1991). The pressure drop over the stage is 2.37, and the large jump is used to mimic the thermodynamic effects of a multi-stage turbine. The turbine design and computational grid are shown in Figure 3.

4. Verification study for the linearized Euler simulation

In this section, computational results verifying the linearized Euler model are reported. Two verification problems which can test the relevant features of the linearized Euler solver for the nozzle-flow simulation in Section 5 are discussed.

4.1. *Acoustic source within a two-dimensional parallel jet flow*

The first verification problem is chosen from the Category 4 benchmark problems in the Fourth Computational Aeroacoustics Workshop on Benchmark Problems (Dahl 2004). The same flow is studied by Agarwal *et al.* (2004). An acoustic source is placed within a two-dimensional plane jet. Its radiated sound propagates and is refracted by the base flow. At the same time, the base flow supports the spatial growth of Kelvin–Helmholtz instability waves. In the near field, the sound measurement is overwhelmed by the pres-

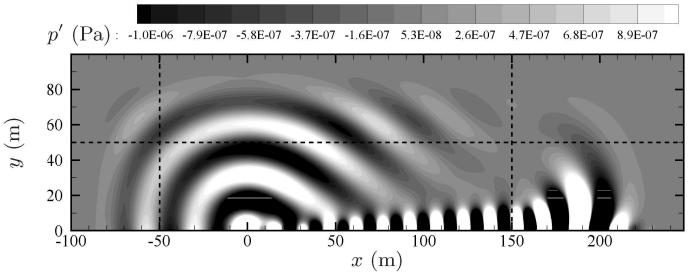

FIGURE 4. Pressure fluctuation contours at the end of the twentieth oscillation period ($tc_\infty/b = 441.6$). The dashed lines represent where the buffer zones start.

sure signature of the instability waves, especially at the aft angles. The objective of this verification problem is to assess if the current model accurately predicts both the direct radiation from the source and the hydrodynamic fluctuations due to the amplified instability waves.

The acoustic source is modeled by a monopole source in the pressure equation ($2.3c$), $f_p = S(\boldsymbol{x})\cos(\omega_0 t)$, and all the other source terms are set to zero. The source distribution is given by $S(\boldsymbol{x}) = A\exp\left\{-(B_x x^2 + B_y y^2)\right\}$, where $A = 0.001$ kgm^{-1}s^{-3}, $B_x = 0.04\ln(2)$ m^{-2}, and $B_y = 0.32\ln(2)$ m^{-2}. The source frequency is $\omega_0 = 76$ rad/s.

The mean velocity profile is parameterized by the centerline Mach number $M_J = 0.756$, the centerline temperature $T_J = 600$ K, and the jet half-width $b = 1.3$ m. The base jet is thus subsonic and heated. The streamwise mean velocity profile is given by

$$\bar{u}(y) = u_J \exp\left\{-\ln(2)(y/b)^2\right\}, \tag{4.1}$$

where $u_J = M_J c_J = 1.07$ and $c_J = \sqrt{\gamma R T_J}$. Since the base jet is parallel, $\bar{v} = 0$. The mean pressure is uniform as $\bar{p} = 103,330$ kgm^{-1}s^{-2}, and the mean density profile is given by the Crocco–Busemann relation as

$$\frac{1}{\bar{\rho}(y)} = -\frac{1}{2}\frac{\gamma-1}{\gamma\bar{p}}\bar{u}(y)[\bar{u}(y) - u_J] + \frac{1}{\rho_J}\frac{\bar{u}(y)}{u_J} + \frac{1}{\gamma\bar{p}}\frac{u_J - \bar{u}(y)}{u_J}. \tag{4.2}$$

The simulation domain is a two-dimensional box consisting of a single block, and the physical domain ranges from $x = -50$ m to 150 m in the streamwise direction and from $y = 0$ m to 50 m in the transverse direction. The symmetry condition is imposed on the centerline at $y = 0$ m. Absorbing buffer zones surround the physical domain with the lengths of 50 m in both the upstream and the far-field directions and 100 m downstream of the physical domain. The grid is uniform in the x-direction as $\Delta x/b = 0.5$ and non-uniform in the y-direction. The grid spacing in the y-direction is $\Delta y/b \approx 0.05$ for $y \leq 15$ m and its maximum spacing is limited to have spatial resolution corresponding to, at least, four points per wavelength. The number of grid points is 429 by 352 in the x- and y-directions, respectively. The time-step size is $\Delta t c_\infty/b = 7.7 \times 10^{-3}$.

Figure 4 shows instantaneous pressure fluctuations at the end of the twentieth oscillation period, corresponding to $tc_\infty/b = 441.6$. The entire simulation domain is shown and the source is located at the origin. The direct radiation of the source is seen especially along the sideline direction, and the instability waves grow in the streamwise direction. Within the absorbing buffer zones, pressure disturbances decay smoothly as they propagate without significant reflections from the domain boundaries.

Figure 5 compares the streamwise distribution of p' at $y = 15$ m. The previous numer-

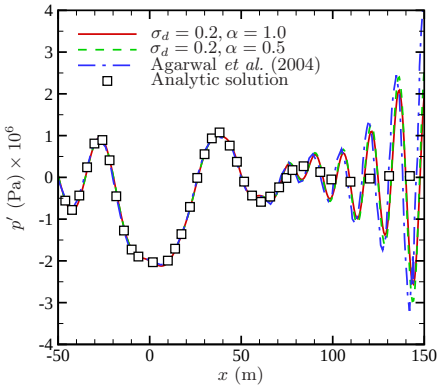

FIGURE 5. Instantaneous pressure fluctuations along $y = 15$ m at the end of the twentieth oscillation period ($tc_\infty/b = 441.6$). The analytic solution is found in Agarwal *et al.* (2004).

ical result by Agarwal *et al.* (2004) and the corresponding analytic solution are shown as well. It was found that the current results are sensitive to the filter-blending parameter α, with $\alpha = 0.5$ giving close agreement with the previous simulation of Agarwal *et al.* (2004). Thus, $\alpha = 0.5$ is used throughout this report. Note that the analytic solution is removed of the hydrodynamic fluctuations using a frequency-domain formulation and thus contains only sound from the acoustic source refracted by the mean flow (Agarwal *et al.* 2004).

4.2. *Acoustic scattering by two rigid cylinders*

The second verification problem also comes from the Fourth Computational Aeroacoustics Workshop on Benchmark Problems (Dahl 2004). The Category 2 benchmark problem is solved to predict the acoustic scattering by two rigid cylinders. Scattered sound waves typically have amplitudes several orders-of-magnitude smaller than those of the original sound waves. Thus, numerical dispersion and dissipation can significantly affect the solution accuracy. Also, the implementation of solid-wall boundary conditions can be assessed, which is important for jet-noise prediction where a nozzle geometry is included. The computational domain is discretized by multiple, overlapping blocks so that the overset-grid capability can be tested.

In the ambient base state, a time-harmonic pressure source located at the origin emits sound waves. The unsteady source strength is given by

$$f_p = (\gamma - 1) \exp\left\{ -\ln(2) \left\{ \frac{x^2 + y^2}{b^2} \right\} \right\} r(t) \sin(\omega_0 t), \tag{4.3}$$

where $\omega_0 = 2\pi/T = 8\pi$ and $b = 0.2$. The function $r(t)$ is given by $\sin^2[(\omega_0 t)/64]$ for $t < 16T$ and 1 for $t \geq 16T$, following Manoha *et al.* in Dahl (2004). This ramps up the magnitude of f_p in time for the initial sixteen oscillation periods.

Two rigid cylinders located the same distance away from the source scatter sound waves. The larger cylinder of diameter $D_{\max} = 1.0$ is centered at $(x, y) = (-4, 0)$ and the smaller cylinder centered at $(x, y) = (4, 0)$ has a diameter of 0.5. Geometric details and overlapping grid configuration are shown in Figure 6. The symmetry condition is imposed on the centerline at $y = 0$ m. An absorbing buffer zone starts from the radial position

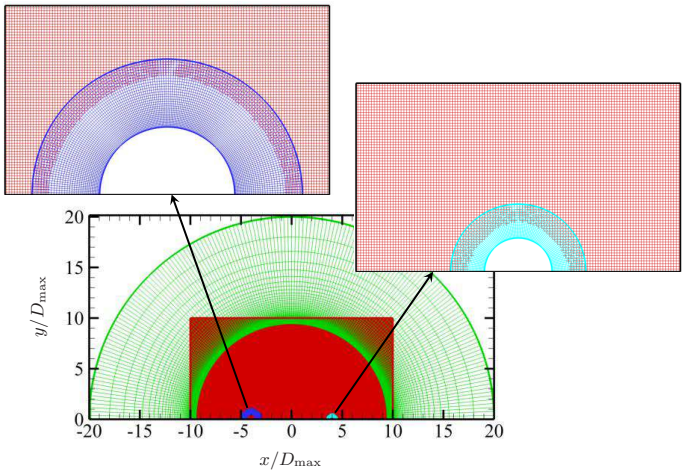

FIGURE 6. Computational domain and overlapping grids for the cylinder scattering problem.

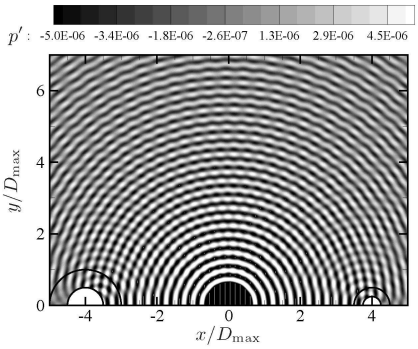

FIGURE 7. Instantaneous pressure fluctuations at $t = 36$. The thick solid lines represent the block interfaces.

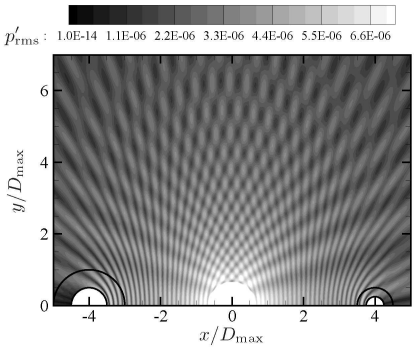

FIGURE 8. Root-mean-square pressure fluctuations. The thick solid lines represent the block interfaces.

of $10D_{\max}$. In total, half a million grid points are used for four overlapping blocks. The time-step size is $\Delta t c_\infty / D_{\max} = 2 \times 10^{-3}$.

Solutions are time advanced for 160 oscillation periods and averaged over the last sixteen periods. Figures 7 and 8 show instantaneous and root-mean-square pressure fluctuations, respectively. The scattered pressure field is well captured, and the impact of the overset-grid interfaces appears insignificant. The scattered field is not symmetric with respect to $x = 0$ since the cylinder diameters are not equal. It was found essential to use the ramping function $r(t)$ in Eq. (4.3); the initial transients due to the non-compact source are much stronger than the small-amplitude scattered waves and the impacts persist even after hundreds of periods.

The centerline distribution of pressure fluctuations is shown in Figure 9. The quantitative agreement is acceptable, and both amplitude and phase of the scattered sound field are well predicted. The pressure distributions on the cylinder surfaces also show good agreement with the analytic solutions, as shown in Figure 10.

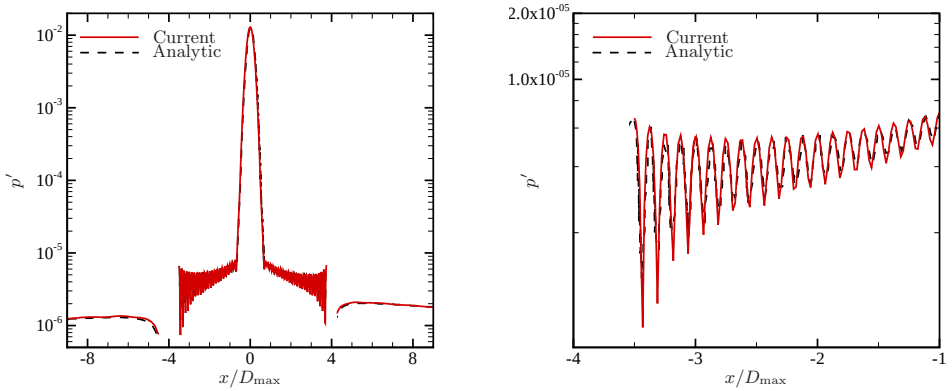

FIGURE 9. Root-mean-square pressure fluctuations along the centerline at $y = 0$ for (a) $-9 \leq x \leq 9$ (the physical domain) and (b) $-3.5 \leq x \leq 1$ (close to the larger cylinder). The analytic solution is taken from Sherer (2004).

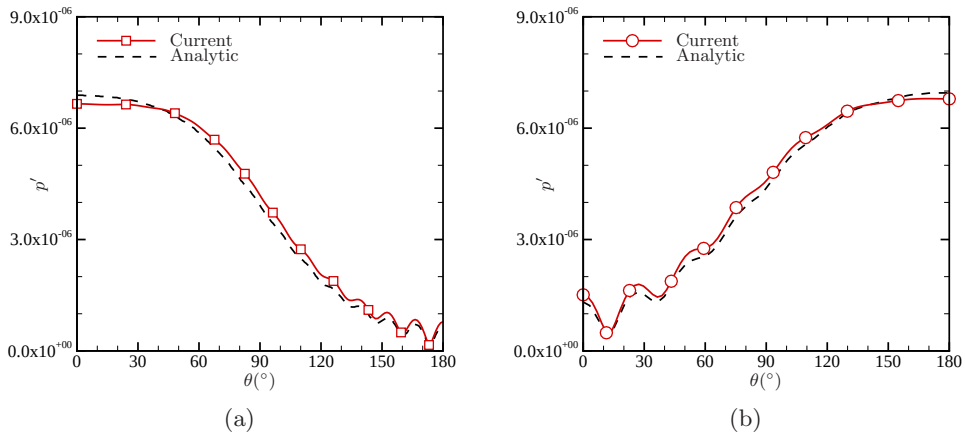

FIGURE 10. Surface pressure fluctuations on (a) the larger cylinder and (b) the smaller cylinder. The analytic solution is taken from Sherer (2004).

5. Response of the subsonic heated jet to time-harmonic excitations

The response of the nozzle base flow to external excitations is examined by solving the linearized Euler equations. The external excitation is prescribed as a time-harmonic plane wave at a fixed frequency. In this study, the linearized Euler simulation is not coupled to the upstream turbine-stage. The results provided here are intended to demonstrate the feasibility of the current linearized Euler model.

An axisymmetric, subsonic heated jet from a converging nozzle is simulated using the linearized Euler model to study its response to external time-harmonic excitations. A schematic of the simulation domain is shown in Figure 11(a). The nozzle radius is denoted by $r_J = 1$ in and used as a reference length. The physical domain extends $50r_J$ downstream of the nozzle exit and $30r_J$ in the radial direction. Absorbing buffer

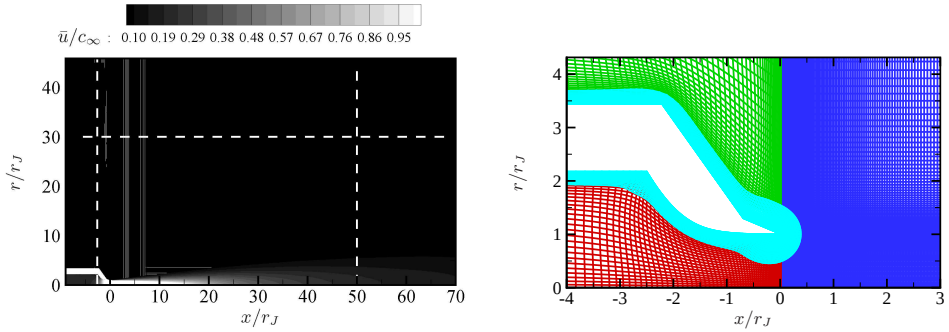

FIGURE 11. (a) Computational domain. The dashed lines represent where the buffer zones start. (b) Overset-grid configuration near the nozzle exit.

zones have the lengths of $6.4r_J$ upstream of the nozzle exit, $20r_J$ downstream of the physical outflow, and $16r_J$ in the radial direction. The converging nozzle is included in the simulation domain using a body-fitted grid, as illustrated in Figure 11(b). The sharp trailing edge of the nozzle lip is rounded to avoid numerical instability. The center of the nozzle exit is $(x, r) = (0, 0)$, which is also the reference point to define the radiation angle φ with $\varphi = 0^\circ$ corresponding to the downstream jet axis. Four overlapping blocks are used to represent the domain, and a total of 10^5 grid points are used. The time-step size is $\Delta t c_\infty / r_J = 10^{-4}$.

The nozzle-exit condition matches the test-point number 49 of Tanna (1977). The non-dimensional velocity at the nozzle exit is $u_J/c_\infty = 1.48$ and the nozzle-exit temperature relative to the ambient temperature is $T_J/T_\infty = 2.857$. The jet Mach number is $M_J = u_J/c_J = 0.876$ and the Reynolds number based on the nozzle-exit condition is $\mathrm{Re}_J = \rho_J u_J D_J/\mu_J = 2.3 \times 10^5$.

A steady RANS simulation is performed to obtain the base state. The computational domain is the same as that of the linearized Euler simulation, and the stagnation condition is specified so that the nozzle-exit condition matches the experiment. Figure 12 shows the centerline profiles of axial velocity and temperature. The agreement in axial velocity with the particle image velocimetry measurement of Bridges & Wernet (2011) is acceptable. The radial profiles shown in Figure 13 also agree well with the measurement. The comparison supports that the current RANS prediction is sufficiently accurate to describe the time-averaged state of the corresponding turbulent jet.

The base flow is perturbed by a time-harmonic plane wave at the nozzle inlet, and the response of the jet is examined. In Figure 14(a), the instantaneous pressure fluctuations of the jet forced at $\mathrm{St}_D = fD_J/u_J = 0.3$ are shown after one acoustic flow-through time. Round jets are most responsive to disturbances at $0.2 \leq \mathrm{St}_D \leq 0.4$, and they produce large-scale, organized vortical structures (Crow & Champagne 1971). Figure 14(a) shows qualitatively similar amplification of large-scale structures and their eventual decay as they convect downstream. The growth–saturation–decay cycle of the convecting wavepackets renders some fluctuations radiation-capable, and strong radiation is observed at the forward angles between $\varphi = 15^\circ$ and 35° (Jordan & Colonius 2013). Compared with Figure 14(b) for the ambient base state, radiation to the sideline angles in Figure 14(a) is dominated by transmitted sound (also refracted by the mean flow). In Figures 15(a) and (b), the responses of the base jet to the excitation at $\mathrm{St}_D = 0.3$ are shown for pressure

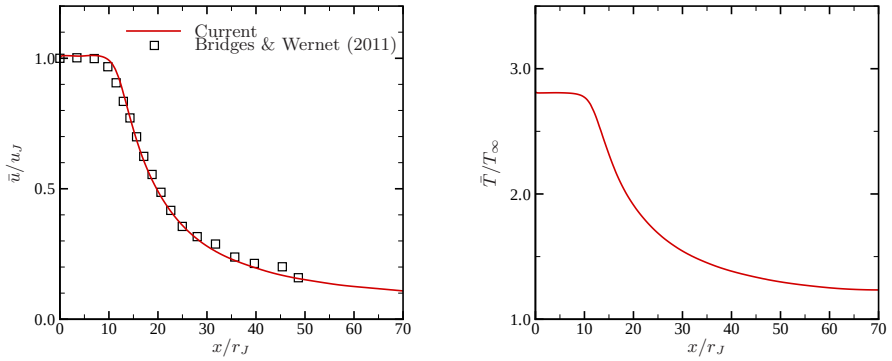

(a) (b)

FIGURE 12. Centerline distribution of (a) axial velocity and (b) temperature.

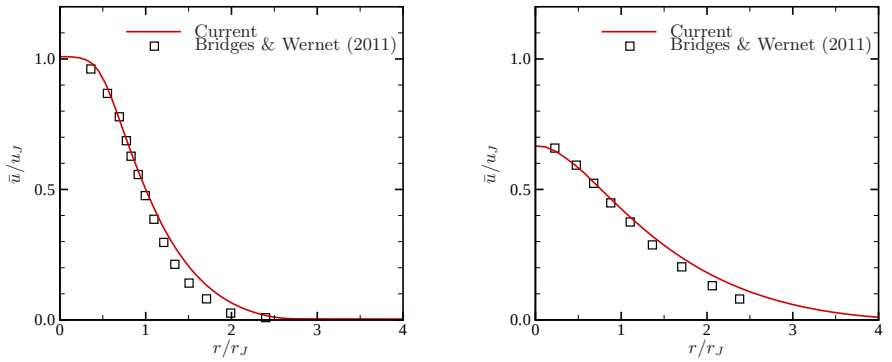

(a) (b)

FIGURE 13. Radial profiles of axial velocity at (a) $x/D = 4$ and (b) $x/D = 8$.

and entropy fluctuations, respectively, followed by Figures 16(a) and (b) for $\mathrm{St}_D = 0.03$. In contrast to the case with $\mathrm{St}_D = 0.3$, the base jet forced at $\mathrm{St}_D = 0.03$ does not show significant amplification of instability waves. In both simulations, no numerical instability is observed near the nozzle-lip region, presumably due to the rounded trailing edge and the high-frequency filter. More detailed analysis on the response of the excited base jet is on-going.

6. Summary and future work

A hybrid modeling approach to predict the engine core noise from a modeled gas-turbine engine and assess its receptivity to time-harmonic excitations is proposed. The modeled core-noise system consists of combustor, turbine, converging nozzle, and free-field radiation to the acoustic far field. The computational strategy for the generation and propagation of turbulent fluctuations from the combustor to the nozzle exhaust is developed. In this report, modeling tools for the individual components are separately developed and tested without coupling.

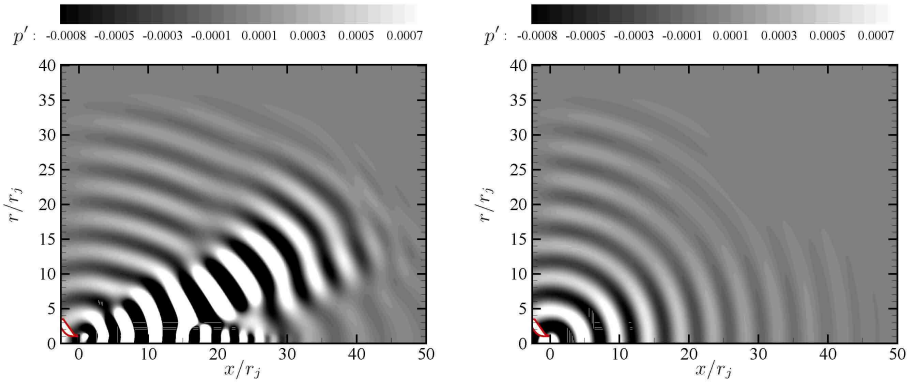

FIGURE 14. Instantaneous contours of pressure fluctuations at $tc_\infty/r_J = 50$ when forced at $\mathrm{St}_D = 0.3$: (a) the RANS-calculated base state and (b) the ambient base state. The nozzle is shown at the lower left corner.

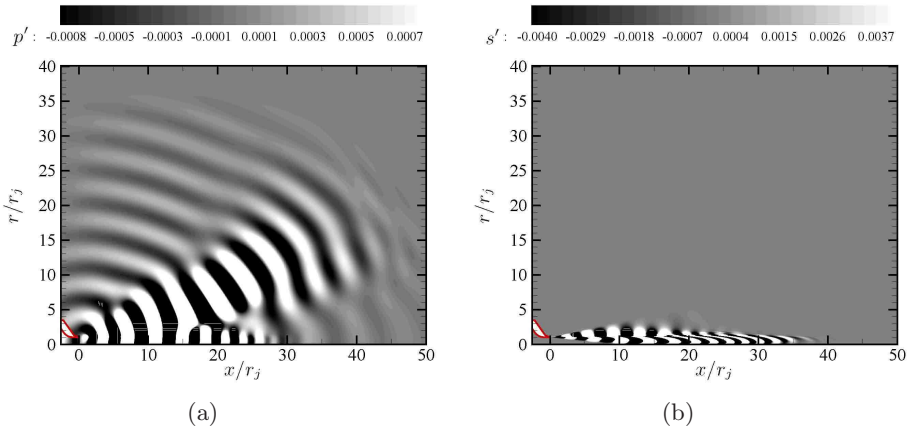

FIGURE 15. Instantaneous contours of (a) pressure fluctuation and (b) entropy fluctuation at $tc_\infty/r_J = 50$. The excitation frequency corresponds to $\mathrm{St}_D = 0.3$. The nozzle is shown at the lower left corner.

To predict the development of near-field disturbances and acoustic radiation to the far field, a linear analysis based upon solving the linearized Euler equations by the high-order optimized finite difference scheme is implemented and verified. The benchmark problems are selected to verify the code's capabilities such as overset-grid interpolation and boundary conditions relevant to the core-noise prediction. The quantitative agreement with the analytic solutions is good. Also, the impact of numerical dispersion and dissipation is carefully assessed for the benchmark problems. Preliminary simulations on the response of the subsonic heated jet to time-harmonic plane waves are performed to demonstrate the feasibility of the linearized Euler model.

Efforts will be made to directly couple the upstream combustor and turbine simulations to provide realistic inflow disturbances to the linearized Euler simulation. In parallel, the linearized Euler model will be assessed independently for the noise-receptivity study. A frequency-response analysis will be performed using the eigenfunctions obtained by the

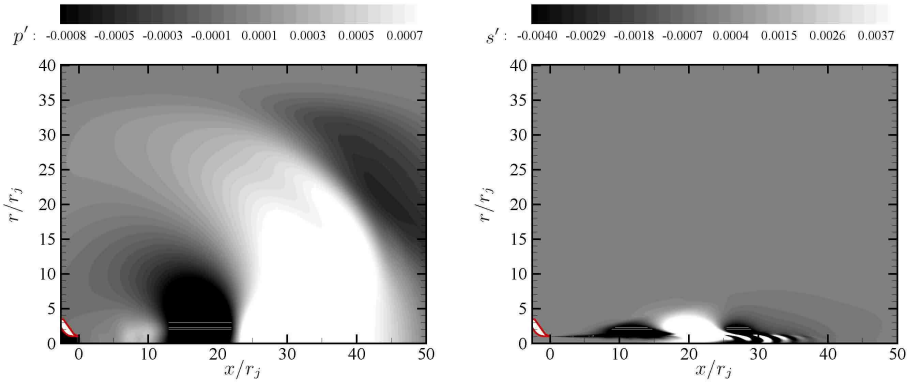

FIGURE 16. Instantaneous contours of (a) pressure fluctuation and (b) entropy fluctuation at $tc_\infty/r_J = 50$. The excitation frequency corresponds to $\mathrm{St}_D = 0.03$. The nozzle is shown at the lower left corner.

spatial stability analysis of the nozzle internal flow. In addition, global analysis is particularly useful for this receptivity analysis in systematically exploring the most receptive frequency and directly identifying the eigenmodes associated with sound radiation at a fixed frequency (Schmid & Henningson 2001; Schmid 2007).

Acknowledgments

The authors acknowledge National Science Foundation for supporting the Certainty cluster at the Center for Turbulence Research which has been used for computing and visualization in this project. The authors are also grateful to Prof. Juan Alonso and Dr. Edwin van der Weide for providing the SUMB code. The second author acknowledges the Stanford Graduate Fellowship program for continued support of this work. The authors would like to thank Dr. Yee Chee See and Prof. Sanjiva Lele for useful discussions.

REFERENCES

AGARWAL, A., MORRIS, P. J. & MANI, R. 2004 Calculation of sound propagation in nonuniform flows: suppression of instability waves. *AIAA J.* **42**, 80–88.

BERLAND, J., BOGEY, C., MARSDEN, O. & BAILLY, C. 2007 High-order, low dispersive and low dissipative explicit schemes for multiple-scale and boundary problems. *J. Comput. Phys.* **224**, 637–662.

BODONY, D. J. 2006 Analysis of sponge zones for computational fluid mechanics. *J. Comput. Phys.* **212**, 681–702.

BOGEY, C. & BAILLY, C. 2004 A family of low dispersive and low dissipative explicit schemes for flow and noise computations. *J. Comput. Phys.* **194**, 194–214.

BRIDGES, J. & WERNET, M. P. 2011 *The NASA subsonic jet particle image velocimetry (PIV) dataset.* NASA/TM–2011-216807.

BROWN, D. L., HENSHAW, W. D. & QUINLAN, D. J. 1999 Overture: Object-oriented tools for overset grid applications. *AIAA Paper 99–3130.*

Crow, S. C. & Champagne, F. H. 1971 Orderly structure in jet turbulence. *J. Fluid Mech.* **48**, 547–591.

Dahl, M. 2004 Fourth Computational Aeroacoustics (CAA) Workshop on Benchmark Problems. NASA CP–2004-212954, Cleveland, OH.

Freund, J. B. 1997 Proposed inflow/outflow boundary condition for direct computation of aerodynamic sound. *AIAA J.* **35**, 740–742.

Hubbard, H. H. 1991 *Aeroacoustics of flight vehicles: Theory and practice,* vol. 1, Noise sources, DTIC Document.

Jordan, P. & Colonius, T. 2013 Wave packets and turbulent jet noise. *Annu. Rev. Fluid Mech.* **45**, 173–195.

Kim, J. W. & Lee, D. J. 2000 Generalized characteristic boundary conditions for computational aeroacoustics. *AIAA J.* **38**, 2040–2049.

Leyko, M., Nicoud, F. & Poinsot, T. 2009 Comparison of direct and indirect combustion noise mechanisms in a model combustor. *AIAA J.* **47**, 2709–2716.

Meier, W., Weigand, P., Duan, X. R. & Giezendanner-Thoben, R. 2007 Detailed characterization of the dynamics of thermoacoustic pulsations in a lean premixed swirl flame. *Combust. Flame* **150**, 2–26.

Motheau, E., Nicoud, F. & Poinsot, T. 2014 Mixed acoustic–entropy combustion instabilities in gas turbines. *J. Fluid Mech.* **749**, 542–576.

Muthukrishnan, M., Strahle, W. C. & Neale, D. H. 1978 Separation of hydrodynamic, entropy, and combustion noise in a gas turbine combustor. *AIAA J.* **16**, 320–327.

Poinsot, T. J. & Lele, S. K. 1992 Boundary conditions for direct simulations of compressible viscous flows. *J. Comput. Phys.* **101**, 104–129.

Schmid, P. J. 2007 Nonmodal stability theory. *Annu. Rev. Fluid Mech.* **39**, 129–162.

Schmid, P. J. & Henningson, D. S. 2001 *Stability and Transition in Shear Flows*. Springer.

See, Y. C., Amini, G., Koh, C. & Ihme, M. 2012 Jet noise receptivity to nozzle-upstream perturbations in compressible heated jets. *AIAA Paper 2012–2259.*

See, Y. C. & Ihme, M. 2014 Large eddy simulation of a partially-premixed gas turbine model combustor. *Proc. Comb. Inst.* **35**, In Press.

Sherer, S. E. 2004 Scattering of sound from axisymetric sources by multiple circular cylinders. *J. Acoust. Soc. Am.* **115**, 488–496.

Stabe, R. G. & Schwab, J. R. 1991 *Performance of a high-work, low-aspect-ratio, turbine stator tested with a realistic inlet radial temperature gradient.* NASA/TM–1991-103738.

Strahle, W. C. 1978 Combustion noise. *Prog. Energy Combust. Sci.* **4**, 157–176.

Tanna, H. K. 1977 An experimental study of jet noise part I: Turbulent mixing noise. *J. Sound Vib.* **50**, 405–428.

van der Weide, E., Kalitzin, G., Schluter, J. & Alonso, J. J. 2006 Unsteady turbomachinery computations using massively parallel platforms. *AIAA Paper No. 2006–421.*